

# RADIOMETRIC CALIBRATION OF DIGITAL PHOTOGRAMMETRIC CAMERA IMAGE DATA

**Birgen Haest**, Research Expert  
**Jan Biesemans**, Research Expert  
**Walter Horsten**, Software Development  
**Jurgen Everaerts**, Project Manager  
Flemish Institute for Technological Research (VITO NV)  
Boeretang 200  
B-2400, Mol, Belgium  
[Birgen.haest@vito.be](mailto:birgen.haest@vito.be)  
[Jan.biesemans@vito.be](mailto:Jan.biesemans@vito.be)  
[Walter.horsten@vito.be](mailto:Walter.horsten@vito.be)  
[Jurgen.everaerts@vito.be](mailto:Jurgen.everaerts@vito.be)

**Nancy Van Camp**, Research Expert  
**Jo Van Valckenborgh**, Research Expert  
Flemish Geographical Information Agency (AGIV)  
Gebroeders Van Eyckstraat 16  
B-9000, Ghent, Belgium  
[Nancy.VanCamp@agiv.be](mailto:Nancy.VanCamp@agiv.be)  
[Jo.VanValckenborgh@agiv.be](mailto:Jo.VanValckenborgh@agiv.be)

## ABSTRACT

Since a few years, digital frame cameras are being used for the recurrent conventional photogrammetric mapping tasks within Flanders (Belgium). As a result, area-wide, but mixed-sensor-type (Ultracam, DMC, ...) time series of digital airborne imagery are emerging. Since only recently, a trend can be observed that this imagery is increasingly used for environmental mapping tasks, such as agricultural acreage estimation, dry matter productivity estimation and mapping of vegetation stress. The algorithms generating such products often need quantitative measurements (i.e. at-sensor radiance or at-surface reflectance instead of a dimensionless digital number). Also, in applications where data from different sensor systems has to be fused, it often becomes inevitable to transform the imagery from digital number to radiance or reflectance. However, in operational photogrammetric environments, only little effort has been put into utilizing the attractive radiometric properties of digital photogrammetric cameras for quantitative remote sensing. In this paper, a typical operational situation is presented: the radiometric calibration of an older image set (Vexcel UltracamD images of 2004) by means of multiple recent in-situ hyperspectral measurements (17 spectra measured in the same period of the year of image acquisition and with the same weather conditions, but in 2008). Several possibilities are evaluated using the empirical line method combined with absolute radiometric preprocessing (i.e. atmospheric BRDF, target BRDF, haze correction), as well as relative radiometric preprocessing (i.e. histogram matching). The different pre-processing methods are not only tested on a stand-alone basis, but the effect of various combinations is also investigated.

## INTRODUCTION

The Flemish Geographical Information Agency (AGIV, [www.agiv.be](http://www.agiv.be)) has the mandate within Flanders (Belgium) to organize and stimulate the optimal use of geographic information within the Flemish community. The main activity within this mandate is the establishment and maintenance of a large-scale reference geographical vector database (GRB) of civil structures (road infrastructure, buildings, parcels, waterways, ...).

For the GRB maintenance, several data input channels exist. At this moment, the vector data of new or altered structures comes from municipal communications through a web-based application and this data is composed of in-situ topographic measurements. Where topographic measurements deliver direct topographic information (i.e.

object-type and object-XYZ), image processing and photogrammetry are indirect measurement methods to extract geometrical and contextual information of spatial objects. So, the measurements are not taken directly on the object itself. However, given the advantages of remote sensing data such as the area-wide data collection, the high data redundancy (overlap within and between the flight lines), the rich semantic and dense positional information and the very high planimetric accuracy, it is speculated that image processing (airborne imaging and LIDAR systems, mobile mapping imaging and LIDAR) will have a prominent role in the GRB update process (not in the initial mapping process, there terrestrial mapping methods will continue to dominate).

When dealing with a photogrammetric production workflow, the huge data volumes involved, imply specific structural and organizational boundary conditions. Aspects as long-term archiving strategies and data preservation, sensor spectral calibration, radiometric calibration and geometric calibration, data compression, algorithmic software component maintenance are unavoidable issues. In order to realize the long-term objectives with respect to these issues, AGIV and The Flemish Institute for Technological Research (VITO, [www.vito.be](http://www.vito.be)) formalized in 2008 a cooperation agreement.

VITO hosts the SPOT-Vegetation processing and archiving facility (CTIV) on behalf of the Belgian Science Policy (BELSPO). The presence of this archive (dating back to 1998) has allowed VITO researchers to gain an important experience with respect to the operational aspects of image processing and archiving facilities. Furthermore, by the VITO research activities with respect to hyperspectral remote sensing (e.g. APEX, Airborne Prism Experiment, <http://apex.vgt.vito.be/>) and UAV-borne earth observation (<http://medusa.vgt.vito.be/>), a thorough understanding is available at VITO with respect to spectral, radiometric and geometric sensor design, sensor calibration, and distributed sensor image processing workflows (Biesemans et al., 2007).

This AGIV-VITO cooperation, backed-up with the academic expertise of the Ghent University ([www.ugent.be](http://www.ugent.be)), the Catholic University Leuven ([www.kuleuven.be](http://www.kuleuven.be)) and the Free University of Brussels ([www.vub.ac.be](http://www.vub.ac.be)) has been activated and initiated during a first integration project from June 2008 to December 2008, which resulted in a prototype distributed image processing workflow for GRB mutation detection. This workflow is focused on a minimization of operator input and consists of a number of sub-workflows, as presented in Table 1. The development activities related to this prototype workflow will be used to pinpoint the bottle-necks with respect to algorithms, algorithm implementations, hardware, software and inter-organizational cooperation and this in preparation of the long-term cooperation towards generic image processing workflows in the framework of the Flemish Geographical Data Infrastructure (GDI) .

**Table 1.** Structure of the prototype workflow for GRB anomaly detection.

<b>Archiving workflow</b>	<ul style="list-style-type: none"> <li>• <b>Calibration Support Tools:</b> Support tools for checking the interior and exterior orientation parameters and the spectral and radiometric calibration.</li> <li>• <b>Archiving:</b> The generation of standardized Level1 HDF5 files (i.e. “archive objects”) from the raw incoming image data (Level0) and image metadata in the framework of long-term archiving strategies. Not all data arrives at Level0. Sometimes, only Level2, Level3 or intermediate image products are available. After the calibration checks, the incoming data is transformed to self-descriptive Level2 or Level3 HDF5 archive objects.</li> </ul>
<b>3D workflow</b>	The automated image-based generation of area-wide DEM and DSM models at a user specified spatial resolution. Data-fusion aspects with LIDAR are not included in this project.
<b>Processing workflow</b>	<p>This workflow is subdivided in three sub-systems:</p> <ul style="list-style-type: none"> <li>• <b>Level1 to Level2 processing workflow:</b> the automated generation of orthorectified and atmospheric corrected single images.</li> <li>• <b>Level2 to Level3 workflow:</b> the automated generation of mosaic products.</li> <li>• <b>Level2/3 to Level4 processing workflow:</b> <ol style="list-style-type: none"> <li>a. the generation of a soft classification based on Level2/3 image data, auxiliary data (DSM, texture parameters, ...) and a GRB that is being used for (a) “field-truth” collection (i.e. classification training data) and (b) as reference map to determine change.</li> <li>b. Modules for interpreting the soft classification and the creation of a change-vector-layer</li> </ol> </li> </ul> <p>HDF5 (<a href="http://www.hdfgroup.org">www.hdfgroup.org</a>) is used for all product packaging and archiving.</p>

The image processing workflow is meant to be deployed on a dedicated cluster (preferably Linux) and can be tuned for either the chain production of standard products from incoming imagery and for an “event-based” processing of customized products. The logical model is presented in Figure 1.

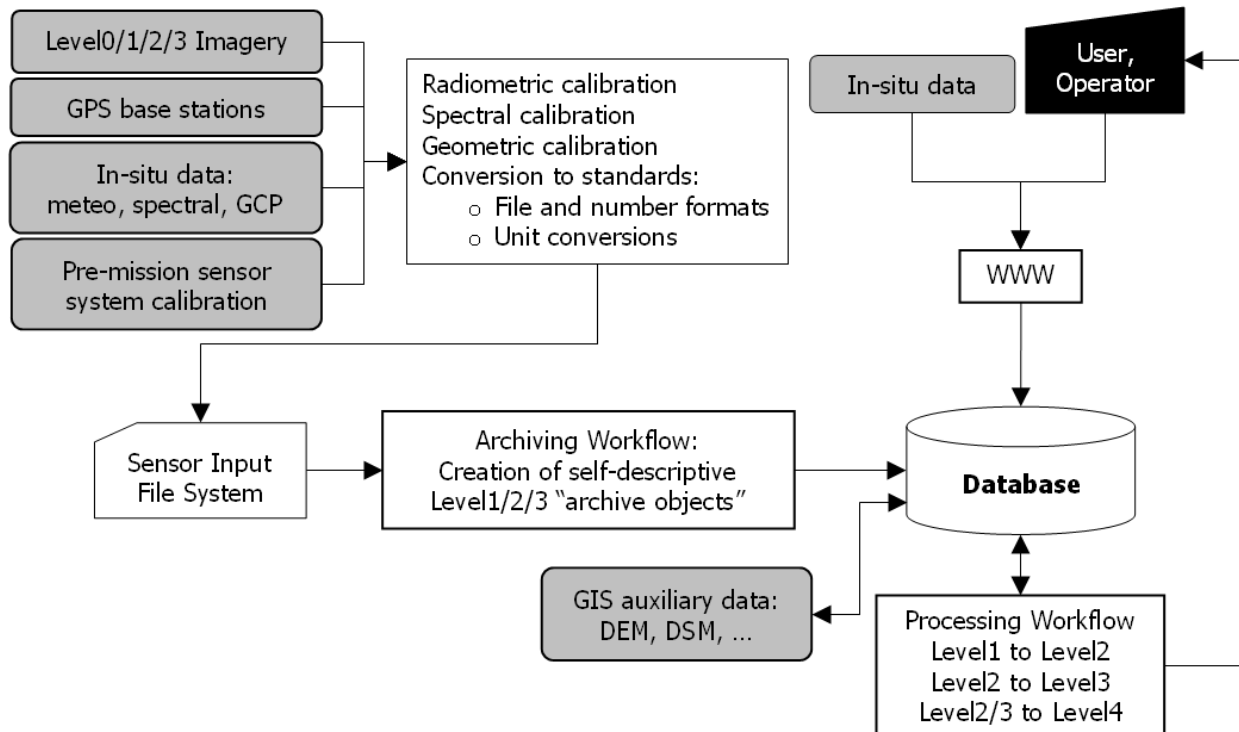


**Figure 1.** Functional flow of the prototype workflow for GRB anomaly detection.

Although the current prototype is focused on photogrammetry (GRB change detection), it is planned to upgrade the system for environmental, agricultural, forestry and ecological mapping applications. The algorithms used in these applications often need quantitative measurements, i.e. radiance or reflectance instead of a dimensionless digital number. Furthermore, for some applications (e.g. recognition of tree species in forestry applications), data fusion of photogrammetric cameras with hyperspectral pushbrooms or whiskbrooms is foreseen. It is clear that a good radiometric calibration of the different sensor systems will enhance the usability and interoperability of the image data. However, for photogrammetric cameras, information about the radiometric properties is very sparse.

Because of (a) the increasing availability, (b) the superior quality of airborne imagery in the spectral, radiometric and geometric domain and (c) because of the ideal meteorological conditions during an airborne mission, there is a trend that imagery from photogrammetric cameras is increasingly being used for environmental applications which traditionally used satellite borne imagery. However, for photogrammetric airborne imagery, the spectral and radiometric calibration is often of poor quality. A frequently reoccurring question from this environmental mapping user segment is thus how to calibrate this imagery radiometrically. When these questions arise, the image data is usually some months to some years old. Then, the calibration exercise has to be executed using spectral field measurements that were not sampled at the same time of the airborne mission. This paper presents the result of such an exercise, where an UltracamD dataset of June 2004 had to be radiometric calibrated using ASD field spectrum measurements of July/August 2008.

## PROPERTIES OF THE STUDY DATA SET

### Properties of the Image Data Set

Vexcel Imaging GmbH ([www.vexcel.co.at](http://www.vexcel.co.at)) brought the large format digital aerial camera UltraCamD onto the market in May 2003. The concept of the sensor is based on combining image data of several CCD sensors and different optical systems to generate one large image. The sensor unit is composed of 8 independent cameras, the so-called optical cones. The imagery of four of these cones are combined to create one large panchromatic image. The other 4 cones, each consisting of one CCD sensor, capture the energy in the blue, red, green and Near-Infrared (NIR) part of the electromagnetic spectrum. The different cameras were designed such that panchromatic and color images have the same resulting field of view (FOV) (Markelin *et al.*, 2005).

**Table 2.** Overview of Vexcel UltraCam D camera main properties

PAN	Image dimensions	11500 x 7500 pixels
	Physical pixel size	9 $\mu\text{m}$ x 9 $\mu\text{m}$
	Focal length (standard)	100 mm
	Aperture	f=1/5.6 – 1/22
	Spectral resolution (nm)	390-690*
Multispectral	Colors	RGB and NIR
	Image dimensions	4008 x 2672 pixels
	Physical pixel size	9 $\mu\text{m}$ x 9 $\mu\text{m}$
	Focal length	28 mm
	Aperture	f=1/4.0 – 1/16
	Spectral resolution (nm):	
	Blue	390-530*
	Green	470-660 <b>Error!</b>
	Red	570-690 <b>Error!</b>
	NIR	670 -940 <b>Error!</b>
General	Year of introduction	2003
	Sensor type	Area CCD
	FOV across track	55°
	FOV along track	37°
	Smallest ground sampling distance	3 cm (at 300 m altitude)
	Forward Motion compensation	TDI
	Maximal frame rate	0.75 sec/image
	Shutter speed options	1/60 - 1/500 sec
	Radiometric resolution	> 12 bit

Vexcel's UltraCam D digital camera system delivers large format aerial imagery that is radiometrically and geometrically superior to images captured by conventional film cameras at a comparable price. Its radiometric resolution is higher than 12-bit per pixel, compared to less than 8-bit per pixel for traditional film cameras which furthermore suffer from grain-noise. Table 2 lists the most important properties of the UltraCam D sensor, and Figure 2 shows the spectral response functions for the PAN and multispectral bands of the camera (Clevers *et al.*, 2005; Markelin *et al.*, 2005; Schiewe, 2005; Honkavaara and Markelin, 2007). The images used in this study were taken over the surroundings of the municipality Brasschaat in the North of Belgium. In total, the applied data set for this calibration exercise consists of 19 images, obtained during a flight mission on June 8, 2004. It was a rather clear day, providing acceptable weather conditions for a photogrammetric mission.

**Table 3.** Properties of study image data set

Sensor	Ultracam D
Acquisition date	June 8, 2004
Acquisition time (GMT)	3:53 PM
Number of images	19
Spatial resolution (cm)	27
DN bit range	16 bit
Solar Zenith Angle (°)	55.50 - 55.60
Solar Azimuth Angle (°)	264.10 - 264.30

\* Various literature sources contradict each other, but in our experience these number are most fit

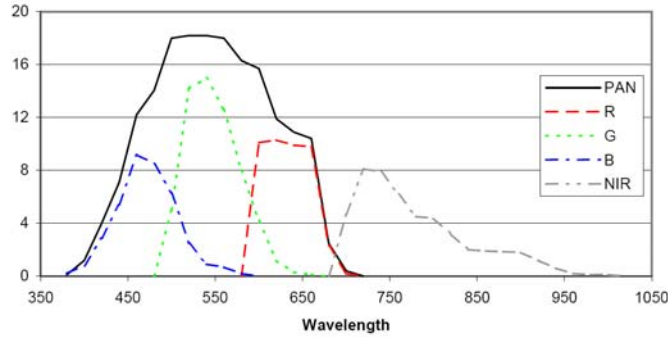


**Figure 2.** Vexcel UltraCam D spectral response functions.

**Table 3.** Properties of study image data set

Sensor	Ultracam D
Acquisition date	June 8, 2004
Acquisition time (GMT)	3:53 PM
Number of images	19
Spatial resolution (cm)	27
DN bit range	16 bit
Solar Zenith Angle (°)	55.50 - 55.60
Solar Azimuth Angle (°)	264.10 - 264.30

As is often the case in an image block data set, the images show large colour differences between the frames (Figure 3) due to various view angle dependent and wavelength dependent BRDF effects. To take this variance into account, it was therefore chosen to take spectral samples at locations that were observed in multiple images.

#### In-situ Data Set

To be able to radiometrically correct images of cameras with no calibration data, in-situ measurements can be a very helpful, if not necessary, tool. More specifically, spectra of easily recognizable objects that are somewhat consistent in time (e.g. a concrete parking lot), are needed to perform radiometric correction using the empirical line method. Both bright and dark targets are necessary to enable the extraction of a meaningful relation. In an ideal case, the in-situ measurements are performed simultaneously with the acquisition of the imagery. For photogrammetric missions, in-situ spectral measurements are usually not foreseen, so one is forced to acquire them at a later time.

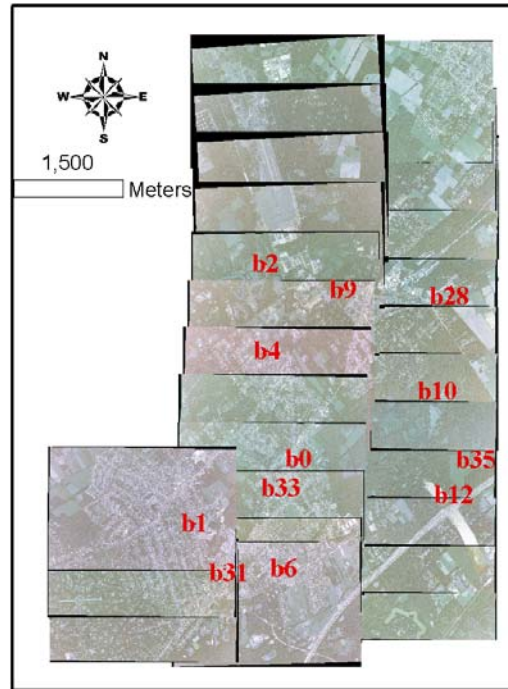
For this study, 17 hyperspectral in-situ measurements of diverse surface covers were taken 1st of July and 6th of August 2008 using an ASD spectroradiometer. The ASD spectroradiometer has an overall range of 350-2500 nm and uses three internal diodes to measure radiation. The first diode is fixed and measures radiation from 350-969 nm. The second and third are scanning diodes and measure incoming radiation from 969-1749 nm and 1750-2500 nm, respectively (Dallon, 2003). Radiance is measured with an interval of 1 nm. By measuring the reflected radiance of a Spectralon panel (white panel that has near-Lambertian reflectance properties) before each target measurement, the albedo (reflectance) values were calculated for each target.

Table 4 and Figure 3 provide an overview of the measurements main properties and locations. The associated measured reflectance spectra can be found in Figure 4 (left). The extreme bias values around 1350 and 1800 nm are due to the transition in the ASD internal diodes, and should hence be ignored. For each target, 9 in-situ measurements were made and averaged. Subsequently, the averaged in-situ measurements were propagated to at-sensor-radiance (ASR) using MODTRAN 4.3. Input parameters for the MODTRAN4.3 model were chosen based on the available information on the UltraCam D flight mission of 2004. Figure 4 (right) shows some examples of the estimated ASR of the in-situ measurements.

**Table 4.** Overview in-situ ASD measurements

ID	X center (Belgian Lambert 1972)	Y center (Belgian Lambert 1972)	Buffered distance (m)	Info
b0	159745.5870	221957.1240	1	Gravel (parking lot)
b0b	159749.9200	221959.1400	1	Gravel (parking lot)
b1	158313.7592	221060.6087	1	Asphalt (Hospital road entry)
b2	159285.2413	224669.5322	1	Parking lot
b4	159315.5484	223460.5931	1	Parking lot
b5	159528.0866	220397.1300	1	Grey bricks
b6	159537.3007	220439.8998	1	Dolomite road
b7	160392.4076	224382.6329	1	Asphalt

b8	160493.1329	224381.0213	1	Asphalt
b10	161673.3074	222896.6052	1	Short trimmed grass area
b12	161906.0514	221461.5777	1	Pasture
b26	161863.7192	224350.8360	1	Asphalt (military domain)
b29	159297.3994	224666.1799	1	Concrete road
b30	158731.3604	220437.8439	1	Asphalt
b31	158784.9649	220379.5106	1	Tiled square
b33	159510.6912	221592.1866	1	Red bricks
B35	162206.7301	221951.4676	1	Grey bricks



**Figure 3.** Overview of the image data set en in-situ measurements.

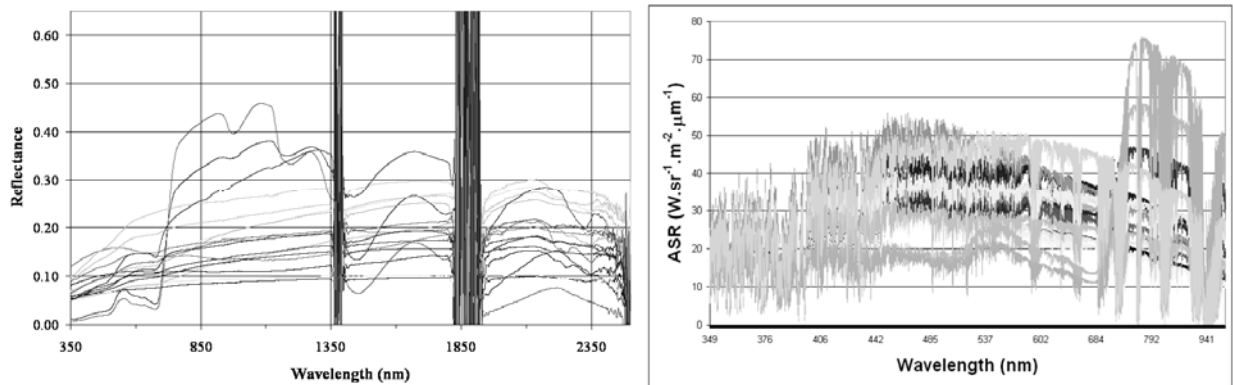


**Figure 4.** Reflectance (left) and at-sensor-radiance spectra of the in-situ measurements.

## ALGORITHM THEORETICAL BACKGROUND

### Empirical Line Method for Radiometric Calibration

Empirical line method is a technique that is often applied to perform an atmospheric correction (i.e. conversion of at-sensor radiance to at-surface reflectance). The principle can however be extended to convert digital numbers (DN) to at-sensor radiance. The method consists of setting up a linear regression between the image DN and the measured reflectance of certain targets. If there is a time gap between the image acquisition date and the ground measurements, the target data set should consist of a set of pixels whose reflectance values do not change significantly throughout the year, or under different solar and atmospheric conditions. The method has the large advantage that it is simple and easy to implement (Liang, 2002).

### Target BRDF Correction

Target BRDF (Bidirectional Reflectance Distribution Function) is the target materials' view angle and wavelength dependent reflectance function. A large number of analytical, empirical and semi-empirical models have been developed to model the bidirectional effects of surface materials (Walthall *et al.*, 1985; Li and Strahler, 1992; Roujean *et al.*, 1992; Wanner *et al.*, 1995; Lucht, 1998). Physical (i.e. analytical) models are the most complex, and since they normally have nonlinear properties, inversion requires many highly accurate observations or a priori knowledge, and has a very high computational load. As a result, the use of physical models is only advisable if one is interested in extracting the bidirectional information itself (e.g. to deduct specific crop properties). In situations where this is not the case (e.g. mosaicing of a block of images), the correction using the (semi-)empirical models is most often sufficient to achieve the objective with acceptable accuracy. (Semi-)empirical BRDF models have linear properties and use fewer model parameters. They are derived from physically based BRDF models, but have a simple linear form (Gao *et al.*, 2003). Although (semi-)empirical models do not result in sun and sensor geometry independent pixel spectra, the objective of their appliance is to normalize all spectra in the image to one standard geometry, being in most cases the at-nadir view and sun angles.

In the last few years, *kernel based* models have gained significant attention to normalize remote sensing data. These models are (semi-)empirical, and based on linear combinations of so-called kernels. Each of these kernels is an angular-dependent function that accounts for part of the angular-dependent reflectance behaviour. In general, such a kernel based model can be mathematically expressed as follows (Hu *et al.*, 1997; Jupp, 2000):

$$\hat{\rho}(\theta_i, \theta_r, \phi, k, \lambda) = f_{iso}(k, \lambda) + f_{vol}(k, \lambda)K_{vol}(\theta_i, \theta_r, \phi, k, \lambda) + f_{geo}(k, \lambda)K_{geo}(\theta_i, \theta_r, \phi, k, \lambda)$$

which represents the modelled/fitted surface reflectance ( $\hat{\rho}$ ) as a function of component reflectance ( $f_x$ ) which depend on the object class ( $k$ ) and the wavelength ( $\lambda$ ), and the kernels ( $K_x$ ) which are mathematical functions that depend on sun (or incident) and view (or observer) angles ( $\theta_i$  and  $\theta_r$ ), relative azimuth angle ( $\phi$ ), object class ( $k$ ) and wavelength ( $\lambda$ ). The subscripts *geo* and *vol* refer to the physical bases for some kernels in which there is an identification of a "geometric" or hotspot factor and a "volume" or path length and scattering factor.  $f_{iso}$  is an object class and wavelength dependent constant that represents the isotropic reflectance. By convention, kernel based models are expressed in such a way that when sun and observer are at-nadir:

$$K_{vol}(0,0) = K_{geo}(0,0) = 0$$

and consequently reflectance  $\hat{\rho}(0,0) = f_{iso}$  (Jupp, 1997; Jupp, 2000). Some of the most commonly used BRDF kernel functions in these models include Ross Thick ( $K_{vol}$ ) (Roujean *et al.*, 1992), Ross Thin ( $K_{vol}$ ) (Wanner *et al.*, 1995), Li Sparse ( $K_{geo}$ ) (Wanner *et al.*, 1995) and Li Dense ( $K_{geo}$ ) (Wanner *et al.*, 1995). The reader is referred to Jupp (2000) and the respective papers for extensive details on these kernel functions.

Wu (2006) presented a kernel based model to eliminate BRDF effects in overlapping aerial photographs and satellite images. To illustrate the principle of the model, assuming there are two overlapping images (left and right), the least-squares model can be written as (other cases can be extended):

$$\begin{cases} v_1 = a_0 + k_{a1}a_1 + k_{a2}a_2 - g_1 & w_1 \\ v_2 = b_0 + k_{b1}b_1 + k_{b2}b_2 - g_2 & , w_2 \\ v_3 = a_0 + k_{a1}a_1 + k_{a2}a_2 - b_0 - k_{b1}b_1 - k_{b2}b_2 - (g_1 - g_2) & w_3 \end{cases}$$

Where  $k_{a1}$  and  $k_{a2}$  are the two kernels for the left image;  $k_{b1}$  and  $k_{b2}$  are the two kernels for the right image;  $a_0$ ,  $a_1$  and  $a_2$  are the fitting coefficients for the left image;  $b_0$ ,  $b_1$  and  $b_2$  are the fitting coefficients for the right image;  $g_1$  and  $g_2$  are the left and right image grey values;  $w_1$ ,  $w_2$  and  $w_3$  are the weights for the three observations; and  $v_1$ ,  $v_2$  and  $v_3$  are the fitting residuals for three observations.

To evaluate the goodness-of-fit of the model, following error is used, with  $n$  the total number of observations:

$$\sigma_0 = \sqrt{\frac{\sum v_i^2}{n-1}}$$

Different BRDF kernel functions can be used in this model, and evaluated for their performance. In this study, following combinations of geometric and volumetric kernels are used: Ross Thick – Li sparse; Ross Thick – Li dense; Ross Thin – Li sparse; and Ross Thin – Li dense. The best performing combination is withheld to apply the BRDF correction.

### Atmospheric BRDF

Viewing the same object from various angles may lead to significant variations of the path scattered radiance component, an effect known as atmospheric BRDF. The targets for in-situ spectral measurements were chosen so that they occur in multiple images. As such, for this study, it was important to take into account this atmospheric BRDF effect when transforming the in-situ measured reflectance to at-sensor radiance. This effect can be simulated by MODTRAN4, since this model takes into account the complete viewing geometry. However, since no measurements were available for the atmospheric condition (visibility, water vapor content) during the time of image acquisition, these parameters are set to default values.

### Haze Correction

When clouds are present in an image, none (or very little) of the underlying earth surface is sensible due to their high optical density. Haze, on the contrary, is the common term used to address the frequently detected presence of a sort of ‘mist’ in the image which does not entirely obscure the observed surface. It can arise from a variety of atmospheric constituents including water droplets, ice crystals or fog/smog particles. The influence of haze on measured radiance varies along the wavelength region under observation, being most pronounced within the visible spectral region (400-700nm) (Richter, 1996; Zhang *et al.*, 2002; Richter, 2007). Presence of haze mostly results in a blue-to-white ‘veil’ in a true colour image.

In Richter (2007) a method is proposed to correct for the added observed radiance due to haze. The algorithm consists of five major steps: (1) Tasseled cap haze transformation to mask out clear and hazy areas (Crist and Cicone, 1984); (2) Calculation of the regression between the blue and red band for clear areas; (3) Determination of a haze optimized transform (HOT) (Zhang *et al.*, 2002); (4) Calculation of the histogram of HOT for the haze areas; (5) Calculation of the new DN. While this technique furnishes very good results over land areas, problems arise with respect to water bodies and urban targets which induce high HOT values that eventually result in overcorrection of these targets.

### Histogram Matching

One of the most often applied relative radiometric correction techniques is histogram matching. Histogram matching determines a lookup table for each image band that causes its histogram to resemble that of a reference image. This reference image is an image that visually conveys good quality, and for which the DN values are representative for the majority of the data set. Basic histogram matching identifies an output DN for each input DN through equating histogram cumulative distribution functions (CDFs). If  $g(y)$  is the CDF for the histogram of a reference image, and  $f(x)$  is the CDF of the histogram to be matched to the reference, then the histogram matching function for each DN is  $g = (f(x))$ . If the histograms have unequal pixel numbers, multiplying by the ratio of the total pixel number in the reference image to that in the subject image scales the histogram matching function. This scaling may negatively affect histogram matching. Extensive areas of very bright or dark pixels can also cause poor histogram matches (Richards, 1993; Helmer and Ruefenacht, 2005).

### PAN Sharpening

Remote sensing sensors are almost always composed of different multispectral bands (e.g. blue, green, red, NIR) as well as a single panchromatic (PAN) band with a higher spatial resolution than the multispectral bands. In an attempt to merge the benefits of both panchromatic (high spatial resolution) and the monochromatic bands (high

spectral resolution), different data fusion techniques have been developed in the past decades (Yocky, 1996; Wald *et al.*, 1997; Garzelli and Nencini, 2007). PAN sharpening is an often applied data fusion method to merge the PAN band with the MS bands to enhance the spatial resolution of the latter. The goal is to make the fused bands the most similar to what the narrow-band MS sensor would image if it had the same spatial resolution as the broad-band PAN.

Image providers, especially with photogrammetric sensors, frequently employ PAN sharpening in advance of the delivery to the user. Moreover, they generally do not provide the algorithmic details of these pre-processing step, although this affects the radiometric properties of the images. Hirschmugl *et al.* (2005), and Markelin *et al.* (2005) found that for UltraCam D images, the PAN-sharpening process clearly changes the DN<sub>s</sub>. In the (PAN-sharpened) high-resolution images, the DN<sub>s</sub> were significantly lower than in the (original) low-resolution images, and the DN<sub>s</sub> dispersed in the high reflectance values clearly more than in the low-resolution images. The green and NIR channels had the worst performance, closely followed by the red channel. For example, in several cases the 70%-reflectance had smaller DN<sub>s</sub> than the 50%-reflectance. The blue channel was affected the least (half of red-channel). According to Hirschmugl *et al.* (2005) the reason for the weak performance of the NIR-channel is that the NIR and PAN-channels have no spectral overlap. Both of these studies hence show that PAN-sharpening deteriorates the colour information.

Bearing in mind the findings of these studies, it can clearly be deduced that PAN sharpening can affect the results of applications making use of the radiometric information in the images, e.g. change detection through NDVI differencing. Therefore, one should always take care when using PAN sharpened images for such purposes.

## **RESULTS AND DISCUSSION**

### **DN Range Diversity**

Several of the in-situ targets can be found in more than one image. In Figure 5 the range of the (median) DN<sub>s</sub> of data targets over multiple images (red band) are plotted. Only the targets that are present in at least 3 images, are included. By looking into the spread in the DN ranges before and after radiometric correction, it can be deduced that haze and BRDF correction, as well as histogram matching significantly reduce the spread in DN of one target over multiple images. All three preprocessing measures hence have the potential to induce a beneficial effect in obtaining a good linear response curve, and reduce the colour variability between the images. Histogram matching appears to be successful in reducing the spread of all targets, while BRDF and haze correction only succeed for certain targets. Analogous results are obtained for the other bands.

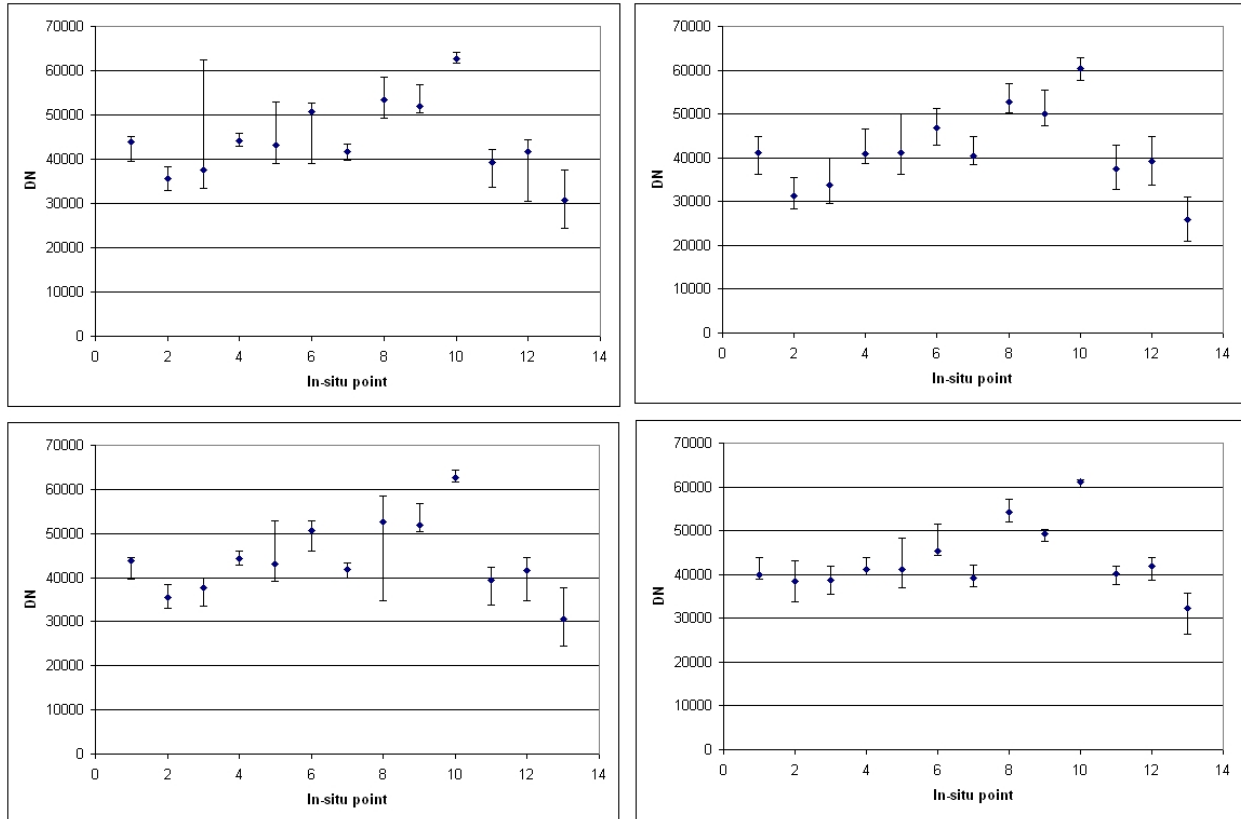


**Figure 5.** Comparison of effect of radiometric preprocessing on DN range of targets in multiple images (red band) (Upper left: Not correction; Upper right: BRDF corr.; Lower left: haze corr.; Lower right: Histogram matching).

### Visual Effects of Haze and BRDF Correction

One of the largest disadvantages of the applied haze correction technique is its bad performance over water bodies. Figure 6. **Detail of an image of the study area showing the negative visual effects of haze correction** shows a detail of a small swimming pool in a true color composite (RGB image) of one of the images of the study area before and after haze correction. It is clearly visible that the correction algorithm has a large negative effect on the radiometry over such small water bodies. Due to an overcorrection in the blue part of the wavelength spectrum, the clear blue colour of the swimming pool has shifted to a dark green. For large water bodies, this overcorrection problem over water bodies can fairly easy be overcome by obtaining a water or land mask using the NIR band, and subsequently masking out the water areas for the haze correction algorithm. For small water bodies (e.g. swimming pools, small ponds), this is however a much more difficult issue. Future research on this matter could target the masking out of the small water bodies to enhance the results.



**Figure 6.** Detail of an image of the study area showing the negative visual effects of haze correction (original: left; haze-corrected: right).

The BRDF correction models described earlier have shown valuable results for lower spatial resolution images (e.g. Landsat, MODIS) (Hu *et al.*, 1997; Danaher *et al.*, 2006). In very high spatial resolution images such as Ultracam D, we notice however unwanted visual effects. In areas of sudden transition between land covers with very distinct reflectance properties, edge effects arise. Figure 7 illustrates this issue for a transition between a bright swimming pool terrace and a dark roof of a building.

It is clear that such apparent effects on radiometry are unwanted and can largely influence the outcome in specific applications involving environmental mapping tasks.



**Figure 7.** Detail of an image of the study area showing the negative visual effects of target BRDF correction

### Radiometric Response of the UltraCam D Images

Figure 8. **Radiometric response plot: without preprocessing (left); after histogram matching (right)** Figure 8 shows the obtained radiometric response plots using all in-situ measurements and their associated DN values without any radiometric preprocessing (left) and after histogram matching (right). For the NIR, the vegetation plots (b10 and b12, cfr Table 4) were left out, because they resulted in extreme outliers. As reflectance of vegetation in the NIR is known to vary largely through time, this was to be expected. For the three bands in the visible part of the spectrum, the vegetation plots however did not appear to cause outlying values.

Both results (as well as other preprocessing measures) indicate a good linearity for all bands. It is however only after appliance of histogram matching that the obtained relative sensitivities (gains of the regression) between the bands match the findings of Honkavaara and Markelin (2007) on radiometric calibration of UltraCam D images. The sensitivity of the NIR and red channel are the highest, with the green channel being less sensitive, followed by the blue channel. For both the red and green channel, saturation seems to occur for at-sensor-radiance higher than  $30\text{-}35 \text{ W}\cdot\text{sr}^{-1}\cdot\text{m}^{-2}\cdot\mu\text{m}^{-1}$ . Further conclusions should however be taken with care, e.g. the obtained regression are only valid for the current image data set, and for the measured at-sensor-radiance range.

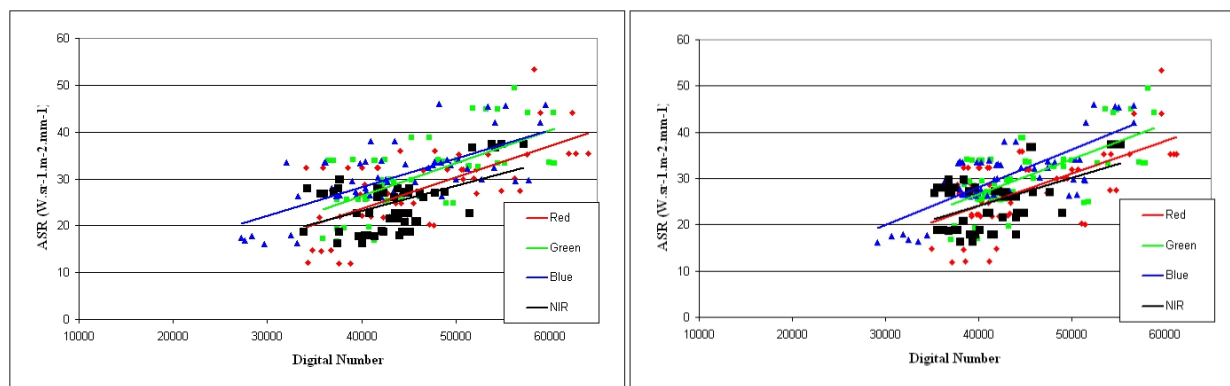


**Figure 8.** Radiometric response plot: without preprocessing (left); after histogram matching (right).

## CONCLUSIONS

In this paper, we have presented the radiometric calibration of an image data set with hyperspectral in-situ measurements dated four years later than the image acquisition time. Although the image data set was characterized by a large number of uncertainties (e.g. unknown filter use and visibility at time of image acquisition), a good linear response could be identified, enabling the radiometric calibration through the empirical line method. Haze and kernel-based-BRDF correction algorithms, as well as histogram matching showed to reduce the data spread of targets across images, and hence induce a beneficial effect in obtaining a good linear response curve, and reduce the colour variability between the images. However, both haze and BRDF correction algorithms result in specific visual deteriorating artefacts that need to be solved before these methods can be successfully introduced in processing chains which have to serve both photogrammetric and environmental mapping user-segments. The study demonstrates the possibility to calibrate the yet existing and future time data series of digital camera images, enabling the merging of image data of different sensors and their use for both photogrammetry and environmental mapping tasks.

## REFERENCES

- Biesemans, J., S. Sterckx, E. Knaeps, K. Vreys, S. Adriaensen, J. Hooyberghs, K. Meuleman, P. Kempeneers, B. Deronde, J. Everaerts, D. Schl pfer, and J. Nieke, 2007. Image processing workflows for airborne remote sensing, In: *5th EARSeL Workshop on Imaging Spectroscopy*, EARSeL, Bruges, Belgium.
- Crist, E.P., and R.C. Cicone, 1984. A physically-based transformation of Thematic Mapper data: The TM tasseled cap, *IEEE Transactions on Geoscience and Remote Sensing*, 22(3):256-263.
- Dallon, D., 2003. Comparison of the Analytical Spectral Devices FieldSpec Pro JR and the Apogee/StellarNet Model SPEC-PAR/NIR Spectroradiometers, Technical Report, Crop Physiology Laboratory, Utah State University.
- Gao, F., Schaaf, C.B., Strahler, A.H., Jin, Y., and Y. Li, 2003. Detecting vegetation structure using a kernel-based BRDF model, *Remote Sensing of Environment*, 86(2):198-205.
- Garzelli, A., and F. Nencini, 2007. Panchromatic sharpening of remote sensing images using a multiscale Kalman filter, *Pattern Recognition*, 40:3568-3577.
- Helmer, E.H., and B. Rufenacht, 2005. Cloud-free satellite image mosaics with regression trees and histogram matching, *Photogrammetric Engineering & Remote Sensing*, 71:1079-1089.
- Hirschmugl, M., H. Gallaun, R. Perko, and M. Schardt, 2005. Pansharpening - Methoden f r digitale, sehr hoch aufl sende Fernerkundungsdaten, *Angewandte Geographische Informationsverarbeitung XVII (Proceedings of AGIT Symposium 2005)* (in German).
- Honkavaara, E., and L. Markelin, 2007. Radiometric Performance of Digital Image Data Collection - A Comparison of ADS40/DMC/Ultracam and EmergeDSS, In: *Photogrammetric Week '07*, pp.117-129.
- Hu, B., Lucht, W., Li, X., and A.H. Strahler, 1997. Validation of Kernel-Driven Semiempirical Models for the Surface Bidirectional Reflectance Distribution Function of Land Surfaces, *Remote Sensing of Environment* 62:201-214.

- Jupp, D.L.B., 1997. Issues in Reflectance Measurement, CSIRO, Earth Observation Centre Discussion Paper, 17p.
- Jupp, D.L.B., 2000. A compendium of kernel & other (semi-)empirical BRDF Models. Office of Space Science Applications - Earth Observation Centre, available only as online document (last accessed November 2008): [www.cossa.csiro.au/tasks/brdf/k\\_summ.pdf](http://www.cossa.csiro.au/tasks/brdf/k_summ.pdf)
- Li, X. and Strahler, A.H., 1992. Geometric-optical bi-directional reflectance modeling of the discrete crown vegetation canopy: effect of crown shape and mutual shadowing, *IEEE Transactions on Geoscience and Remote Sensing*, 30:276-292.
- Liang, S., 2002. Atmospheric Correction of Optical Remotely Sensed Imagery, APEIS Capacity Building Workshop on Integrated Environmental Monitoring of Asia-Pacific Region 20-21 September 2002, Beijing, China
- Lucht, W., 1998. Expected retrieval accuracies of bi-directional reflectance and albedo from EOS-MODIS and MISR angular sampling, *Journal of Geophysical Research*, 103, pp.8763- 8778.
- Markelin, L., E. Ahokas, E. Honkavaara, E. Kukko, and J. Peltoniemi, 2005. Radiometric quality comparison of UltraCam-D and analog camera, *The International Archives of the Photogrammetry, Remote Sensing and Spatial Information Sciences*, 34, Part XXX.
- Richards, J.A., 1993. *Remote Sensing Digital Image Analysis*, An Introduction. Springer-Verlag, New York, USA, 340p.
- Richter, R., 1996. Atmospheric correction of satellite data with haze removal including a haze/clear transition region, *Computers & Geosciences*, 22(6): 675-681.
- Richter, R., 2007. Atmospheric/Topographic correction for Airborne Imagery, ATCOR-4 User Guide, Version 4.2. DLR, Wessling, Germany, 125p.
- Roujean, J.-L., M. Leroy, and P.Y. Deschamps, 1992. A bi-directional reflectance model of the Earth's surface for the correction of remote sensing data, *Journal of Geophysical Research*, 97:20455- 20468.
- Schiewe, J., 2005. Status and future perspectives of the application potential of digital airborne sensor systems, *International Journal of Applied Earth Observation*, 6:215-228.
- Vexcel Imaging GmbH, Münzgrabenstraße 11, A-8010 GRAZ, [www.vexcel.co.at](http://www.vexcel.co.at)
- Yocky, D.A., 1996. Multiresolution wavelet decomposition image merger of landsat thematic mapper and spot panchromatic data, *Photogrammetric Engineering & Remote Sensing*, 62(9):1067-1074.
- Wald, L., T. Ranchin, and M. Mangolini, 1997. Fusion of satellite images of different spatial resolutions: assessing the quality of resulting images, *Photogrammetric Engineering & Remote Sensing*, 63(6):691-699.
- Walthall, C.L., J.M. Norman, J.M. Welles, G. Campbell, and B.L. Blad, 1985. Simple equation to approximate the bi-directional reflectance from vegetation canopies and bare soil surfaces, *Applied Optics*, 24:383- 387.
- Wanner, W., X. Li, and A.H. Strahler, 1995. On the derivation of kernels for kernel-driven models of bidirectional reflectance, *Journal of Geophysical Research*, 100:21077-21090.
- Wu, X., 2006. A BRDF Calibration Approach for Aerial Photographs and Satellite Images, CSIRO Mathematical and Information Sciences, Technical Report 06/85, 14p.
- Zhang, Y., B. Guindon, and J. Cihlar, 2002. An image transform to characterize and compensate for spatial variations in thin cloud contamination of Landsat images, *Remote Sensing of Environment*, 82(2-3):173-187.